Electrochemical kinetics as a function of transition metal dichalcogenide thickness

Marc Brunet Cabré,[1] Aislan Esmeraldo Paiva,[1] Matěj Velický,[2,3,4] Paula E. Colavita,[1] Kim McKelvey[1,5*]

[1]School of Chemistry, Trinity College Dublin, Dublin 2, Ireland.

[2]School of Physics and Astronomy, University of Manchester, Oxford Road, Manchester, M13 9PL, United Kingdom.

[3]Department of Chemistry and Chemical Biology, Cornell University, Ithaca, New York, 14853, United States.

[4]J. Heyrovský Institute of Physical Chemistry, Czech Academy of Sciences, Dolejškova 2155/3, 182 23 Prague, Czech Republic.

[5]School of Chemical and Physical Sciences, Victoria University of Wellington, Wellington 6012, New Zealand.

*kim.mckelvey@vuw.ac.nz

ABSTRACT:

Two-dimensional transition metal dichalcogenides are used as electroactive materials for electrochemical and electrocatalytic applications. However, it remains unclear how transition metal dichalcogenide thickness influences the electrochemical response measured at its surface. We use scanning electrochemical cell microscopy to assess the electrochemical response of different thicknesses of bottom-contacted MoS_2, $MoSe_2$, WS_2, and WSe_2 towards the simple outer-sphere redox couple $[Ru(NH_3)_6]^{3+/2+}$ with submicron spatial resolution. A detailed analysis, coupling mass transport and electrochemical kinetics, reveals that the electrochemical response can be described using an electron tunneling barrier, which scales with the band gap of the two-dimensional transition metal dichalcogenide. Our results suggest that interpretation of the electrochemical and electrocatalytic responses on transition metal dichalcogenide-covered electrodes should account for the through-layer electron transport kinetics.

TOC:

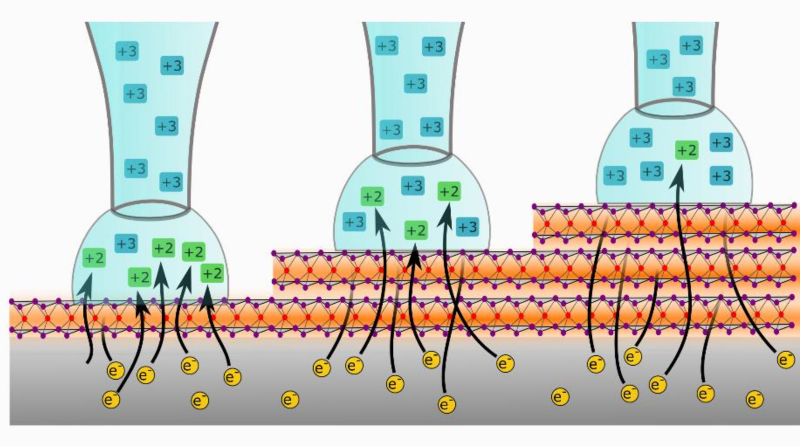

KEYWORDS: TMDC, 2D, thickness dependence, electron transfer, tunneling, SECCM

1. Introduction

The layered crystal structure of transition metal dichalcogenides (TMDCs) enables their mechanical exfoliation into mono- and few-layer two-dimensional (2D) sheets. 2D TMDCs have unique electronic, chemical, and mechanical properties [1], which have been harnessed in electronic, spintronic, photonic, and energy conversion technologies [2–6]. Of particular interest here is the use of 2D TMDCs as active materials for electrochemical and electrocatalytic applications [7–9]. Examples of 2D TMDCs used in electrochemical applications include electrode materials for Li-ion batteries [10], electrodes for supercapacitors [11,12], and electrocatalysts for the hydrogen evolution reaction (HER) [8, 13–16].

The electrochemical response of bulk TMDCs has previously been shown to differ significantly between two distinct surface types: the basal plane and the edge plane [17,18]. Outer-sphere redox mediators, such as hexammineruthenium $[Ru(NH_3)_6]^{3+/2+}$, which we consider here, showed enhanced electron transfer kinetics on the edge plane compared to the basal plane surfaces [17,18]. Similar enhancement of the HER kinetics on the edge planes of MoS_2 crystal compared to its basal plane has also been observed [19].

The preparation of TMDCs in their 2D form typically yields heterogeneous samples with a variable flake size and variable flake geometry. The number of TMDC layers stacked strongly affects the electronic structure and the electrochemistry of the stacked material [7,20,21]. Isolation and electrochemical investigation of specific TMDC thicknesses remain a significant challenge, primarily because it is difficult to prepare homogeneous mono- and few-layer flakes larger than tens of microns in lateral size. This challenge has recently been overcome by a gold-mediated exfoliation of TMDCs, capable of producing millimeter-to-centimeter sized monolayer flakes, combined with localized electrochemical methods [20,22,23].

Scanning electrochemical probe microscopy techniques are particularly well suited to isolate the electrochemical activity of nano- and micro- scale domains [20,24,25]. Scanning electrochemical cell microscopy (SECCM) allows electrochemical mapping with a spatial resolution of tens to hundreds of nanometers using a nanodroplet-electrochemical cell located at the end of a nanopipettes [26–28]. A key advantage of a SECCM approach is the localized measurement at the area of interest, without electrochemical activation of the entire sample surface by its exposure to the electrolyte, as is the case in macroscale electrochemistry or scanning electrochemical microscopy. Furthermore, SECCM can be combined with complementary microscopy approaches, such as atomic force microscopy (AFM), to correlate the electrochemical activity with surface morphology. Unwin *et al*. have previously studied the electrocatalytic activity of bulk TMDCs using SECCM [29,30]. These studies investigated HER on the surface of top-contacted TMDCs (MoS_2 and WS_2), which showed an enhanced electrocatalytic activity at the edge plane compared to the basal plane. Takahashi *et al*. recently used SECCM with an impressive 20 nm resolution to characterize a few-layer MoS_2, as well as heterostructures of MoS_2 and WS_2, confirming an increased HER activity at the edge planes of MoS_2 but showing no significant differences in HER activity on different number of TMDCs layers [31].

We have previously measured the electrochemical and photoelectrochemical response of 2D MoS_2 on an insulating substrate towards reduction of the $[Ru(NH_3)_6]^{3+/2+}$ redox couple using a microdroplet electrochemical cell [32]. This showed the significant effect of the number of layers (comparing monolayer, 3-4 layers, 5-10 layers, and bulk) on the electrochemical response, which was also sensitive to illumination. However, the spatial resolution was limited to the size of the microdroplets (20–40 μm), which made measurements on individual layers challenging. In addition, the electrical contact to the MoS_2 was made directly at the top layer (top-contacted), which we will show to be a key difference with respect to our current results.

The location of the electrical contact made to the 2D TMDCs strongly influences the electrochemical response we observe. In a top-contact configuration, the electrical contact is made to the top layer of the layered 2D material stack, usually using a conductive adhesive and a metallic wire. In this configuration, only lateral electron transport along the layers occurs due to the high in-plane electrical conductivity through the basal plane [33]. In a bottom-contact configuration, electrical contact is established through the supporting metallic substrate on which the 2D layers are immobilized. In this configuration, electron transport occurs between the metallic substrate and the top 2D layer, where the electrochemical reaction takes place. Therefore, in a bottom-contacted sample, the interlayer electron transport can influence the electrochemical response, as we observe in our studies here.

The HER response of monolayer (1L), bilayer (2L), and trilayer (3L) MoS_2 in a bottom-contact configuration has recently been reported [25]; these results revealed that the electron transport between the conductive substrate and 2D TMDC could be the rate-limiting step in HER electrocatalysis. Another work on bottom-contacted MoS_2 suggests that HER electrocatalysis relies on electron hopping between the MoS_2 layers [21]. However, a recent report of HER on bottom-contacted MoS_2 did not observe any significant dependence of the electrocatalytic response on the thickness [31]. Therefore, a clear scientific question arises about how do the layer thickness of TMDCs and the bottom-contact affect the electrochemical response [34]. HER is an inner sphere multistep reaction whose overall rate on TMDC electrodes is proposed to depend on chemical steps involving surface-adsorbate intermediates. Therefore, a well-defined outer-sphere redox couple, sensitive only to the density of electronic states, is better suited to assess the dependence of the electrochemical response on the number of TMDC layers.

To that end, we isolated the electrochemical response from the $[Ru(NH_3)_6]^{3+/2+}$ outer-sphere redox couple on monolayer, bilayer, and trilayer MoS_2, $MoSe_2$, WS_2, and WSe_2, immobilized on an Au substrate. As shown in Figure 1A, a Park Systems NX10 instrument was used to perform both optical characterization, determination of surface morphology by AFM, and the SECCM measurements. We use a SECCM probe with ca. 800 nm spatial resolution to perform the electrochemical mapping, targeting TMDC layers of different thicknesses, as shown in Figure 1B. The electrical bottom contact is established through the Au electrode substrate, as shown in Figure 1C. The localized electrochemical response was then correlated with the surface morphology, characterized by optical microscopy and AFM. We used the Gerischer formalism of electron transfer coupled with the diffusional transport of $[Ru(NH_3)_6]^{3+/2+}$ in the SECCM probe to simulate the electrochemical response. We extract the electron transfer kinetics of the $[Ru(NH_3)_6]^{3+/2+}$ redox couple on the different TMDC thicknesses by fitting simulations to experimental data.

2. Experimental

Hexaammineruthenium (III) chloride ($[Ru(NH_3)_6]Cl_3$) was purchased from JMC Corporation (South Korea). Potassium chloride (KCl, ≥ 99.5%) was obtained from VWR Chemicals (USA). All chemicals were used as received. Distilled water with a resistivity of 18 MΩ cm was used to prepare the solution of 10 mM KCl and 1.0 mM $[Ru(NH_3)_6]^{3+}$. All the procedures were carried out at room temperature.

Samples of the transition metal dichalcogenides (MX_2, M = Mo or W and X = S or Se) were prepared via mechanical exfoliation of bulk crystals on Au substrates, as previously reported [20]. The bottom-contact electrical connection to the TMDCs was established via the gold substrate.

Optical, AFM, and SECCM measurements were acquired on a Park NX10 (Park Systems, South Korea). The AFM images were obtained in a non-contact mode (NCM) with a PPP-NCHR cantilever type (force constant = 42 N/m, resonance frequency = 330 kHz, Nanosensors).

The SECCM probes were made of single-barreled nanopipettes with 300 – 600 nm aperture radius. The nanopipettes were fabricated from single-barreled borosilicate capillaries (1.5 mm O.D and 0.86 mm I.D., BF150-86-7.5, Sutter Instrument, USA) using a P-2000 laser puller (Sutter Instrument, USA). The nanopipette was filled with the solution of 1 mM $[Ru(NH_3)_6]^{3+}$ in 10 mM KCl (sufficient supporting electrolyte for nanoscale electrochemical measurements [35]) using a pipette filler (MicroFil MF34G-5, World Precision Instruments, USA); prior to this, the electrolyte was filtered through a 0.45 µm syringe filter (PTFE membrane, Fisher Scientific, USA). An Ag/AgCl reference electrode was inserted into the top end of the nanopipette.

The SECCM measurements were performed using the ParkSystem NX10 system. The SECCM probe was aligned to the sample area on the surface using the optics and LSVs were then recorded at a preprogrammed squared grid, with individual measurement spots spaced at 1.5 µm. A hopping mode was used in which the probe was approached vertically towards the sample surface at a speed of 0.3 µm/s and a potential of –0.8 V until contact between the nanopipette droplet and the surface was established. The contact was detected as the appearance of a double layer charging current and immediate $[Ru(NH_3)_6]^{3+}$ reduction, with a threshold of 5 pA. At this point, the vertical movement of the probe was stopped immediately, and LSVs were recorded in the potential range of + 0.2 V to –0.8 V at a speed of 1 V/s. After completing the measurement, the nanopipette was retracted and moved to the next sample point on the grid

Simulations of the nanoelectrochemical cell at the end of the SECCM probe were performed in COMSOL Multiphysics (COMSOL 5.2, Sweden). See supplementary information (SI-4) for further details.

3. Results and discussion

3.1 TMDC thickness characterization

Mechanical exfoliation was used to isolate high-quality 2D flakes of MoS_2, $MoSe_2$, WS_2, and WSe_2 on an Au substrate [20]. Regions of the Au substrate coated with TMDC flakes of a different number of layers could be distinguished optically, as shown for $MoSe_2$ in Figure 2A. The optical contrast and color of the flakes change with the different number of layers of $MoSe_2$ [36]. Similar results were obtained for MoS_2, WS_2, and WSe_2, as reported in the Supporting Information (Figures S1-S3).

The optical images were therefore used to locate surface regions containing various TMDCs thicknesses (1L-3L) prior to SECCM characterization. AFM was used to corroborate the layer assignment from the step-height profiles obtained after the SECCM measurement, as shown in Figure 2B. Step-height profiles of 1L/2L and 2L/3L areas displayed in Figure 2C and 2D yield monolayer thickness of *ca.* 0.81 nm and 0.78 nm, in agreement with previous monolayer MoS_2 estimates from AFM (~0.85 nm) [37]. The step-height from Au to 1L could not be clearly determined due to the roughness of the gold surface. AFM step-height profiles for the MoS_2, $MoSe_2$, and WSe_2 samples are displayed in Figure S1 - S3. The measured layer thicknesses agree with previous studies of different TMDCs and support our optical analysis [20,38–40].

3.2 Local electrochemical measurements

SECCM imaging was carried out using a single-barreled nanopipette probe of approximately 800 nm diameter. An Ag/AgCl wire immersed in the electrolyte solution was used as a reference electrode. Linear sweep voltammograms (LSVs) for the reduction of $[Ru(NH_3)_6]^{3+}$ to $[Ru(NH_3)_6]^{2+}$ were obtained at a regular grid of sample points spaced at 1.5 μm intervals on all four TMDC materials (MoS_2, $MoSe_2$, WS_2, WSe_2); multiple measurements were carried out on each surface type (Au, 1L, 2L, and 3L). The AFM images shown in Figure 2B, which were obtained after the SECCM measurements, reveal salt residues left at points of contact between the SECCM droplet and the surface after water evaporation.

The droplet/surface contact area was estimated from the AFM images by measuring the diameter of the droplet residue; these values are summarized in Figure S4. The droplet size is determined by the pipette aperture, with a small variability expected due to the nature of the pipette pulling process. A new pipette was used for each experiment, thus, the average droplet size was slightly different for each of the TMDC materials investigated and estimated to be 0.81 ± 0.05 μm, 0.73 ± 0.05 μm and 0.80 ± 0.09 μm for $MoSe_2$, WS_2, and WSe_2, respectively, as shown in Figure S4. The average droplet size of MoS_2 was found to be considerably larger at approximately 1.30 ± 0.11 μm in diameter. The larger droplet size observed on MoS_2 is due to a larger pipette aperture for this experiment (determined from the diffusion-limited current on MoS_2, see section SI-6). The droplet size displayed only a narrow dispersion with the TMDC thickness, as seen in Figure S4 histograms, while the variance observed is consistent with the wetting behaviour of TMDCs surfaces after exposure to air [41,42]. Grid points sampled on bare gold surfaces (see $MoSe_2$ and WSe_2 samples in Figure S6 – S7) exhibited the largest droplet contact size, which can be attributed to the higher hydrophilicity of Au in comparison to TMDC [42,43].

The salt residues were used to assign each LSV to a specific surface type: bare gold, 1L, 2L, 3L, and layer boundaries. Figure 3A shows an AFM image of a WS_2 sample recorded after the SECCM measurements, where the sampled areas are color-coded to reflect the corresponding surface type, as identified by optical microscopy and AFM. The same protocol was used for the assignment of LSV curves of $MoSe_2$ and WSe_2, as shown in Figures S6 – S7. The relative spacing (1.5 μm) of the SECCM point grid was identical for all four TMDCs. Due to the greater wetting on MoS_2, a larger fraction of the sample became covered by salt residues, which rendered the AFM analysis of the surface type unreliable. We therefore employed optical microscopy to assign the surface type as detailed in Figure S8.

The above procedure resulted in multiple LSV curves obtained at each surface type (Au, 1L, 2L, and 3L), thus generating a representative dataset for further analysis. Both AFM and optical microscopy indicate that several LSVs measurements were obtained at boundaries between different layer thicknesses (such as Au-1L, 1L-2L, Au-2L, 1L-3L boundaries). However, the dearth of data from the boundaries prevents us from drawing any strong conclusions and we leave the analysis of these types of measurement to future work. The AFM imaging also revealed various forms of defects and surface irregularities, such as cracks in the 2D flakes and defects in the underlying Au substrate, as shown in Figure S5-S7. As these defects are likely to affect the electrochemical response, the corresponding LSVs curves were also discounted from the analysis of the electrochemical response as a function of the TMDC thickness, details on the excluded points are given in Table S1.

The TMDC thickness (1L, 2L, 3L) for each point used in our LSV analysis is displayed in Figure 3B for WS_2 and in Figure S6 – S8 for $MoSe_2$, WSe_2, and MoS_2. The LSVs corresponding to 1L, 2L, and 3L WS_2 are shown as black traces in Figure 3C, 3D, and 3E, respectively, while the LSVs on MoS_2, $MoSe_2$, and WSe_2 are shown in the Figures S9-S12. Figures S9 – S12 also show every LSV measurement on TMDCs (including the measurements at defect sites) and LSV measurements once sites with defects have been excluded. Both LSV datasets show the dependence of the electrochemical behavior on the TMDC layer thickness. However, the LSVs collected at the defect sites are noticeably different to those at the pristine basal plane and resemble the Au surface response (Figure S16). The defective areas generally show faster apparent kinetics. One therefore expects macroscopic measurements over both the pristine and defective areas would also yield enhanced kinetics, subject to the defect density.

3.3 Electrochemical kinetics

The LSVs in Figures 3C-3E show that the $[Ru(NH_3)_6]^{3+}$ reduction is more facile on thinner WS_2; similar trends are observed for the other three TMDC materials (Figure S10 - S12). To quantify the observed electrochemical response, a finite element simulation implemented by COMSOL Multiphysics was used to describe the transient diffusional transport of $[Ru(NH_3)_6]^{3+/2+}$ in the SECCM probe (details in section SI-5) and the electron transfer kinetics at the sample surface. The geometry of each SECCM probe used, such as the droplet contact area and pipette aperture, were derived from AFM imaging and limiting current calculations, respectively (see section SI-2 and SI-6).

The simulated rate of heterogeneous electron transport (HET) was described by a Gerischer formalism. As theoretically predicted by Feldberg [44] and recently verified experimentally [45], for an ultramicroelectrode with slow kinetics a significant difference exists between the HET rate constant value calculated from the Butler-Volmer and Marcus-Hush/Gerischer formalism. In the Gerischer formalism, the kinetics of HET can be described by considering the overlap between isoenergetic electronic states of the electrode and the redox species in solution (electronic coupling in the Marcus-Hush formalism). Therefore, the kinetics of cathodic electron transfer (k_{cat}) is given by the overlap between isoenergetic occupied states at the electrode ($f(E)_{occupied}$) and empty electron acceptor states in the solution (W_{ox}) [46]. Likewise, the anodic kinetics (k_{an}) is determined by the overlap of isoenergetic filled electron donor states (W_{red}) in the solution and unoccupied states in the electrode ($f(E)_{unoccupied}$). Therefore, the cathodic and anodic kinetic rates can be written as:

$$k_{cat} = k_{max} \cdot \int_{-\infty}^{\infty} W_{ox}(E) \cdot f(E)_{occupied} \, \partial E \qquad \text{(Eq. 1)}$$

$$k_{an} = k_{max} \cdot \int_{-\infty}^{\infty} W_{red}(E) \cdot f(E)_{unoccupied} \, \partial E \qquad \text{(Eq. 2)}$$

where the integration parameter E is the electron energy (in eV), and the prefactor, k_{max}, is the maximum rate of electron transfer [46]. The solution states (W_{ox} and W_{red}) are described by normalized Gaussian distributions and the electrode states ($f(E)_{occupied}$ and $f(E)_{unoccupied}$) are described by normalized Fermi-Dirac distributions for free electrons in a metal, see supplementary information (SI-7) for more details.

The overlap integrals for anodic and cathodic processes, as described in Eq.1 and Eq.2, were calculated by numerical integration, obtaining two waveforms (for anodic and cathodic processes), which describe the ratio of the overlap of the reacting redox species as a function of the applied potential. The waveforms, displayed in Figure S15, range between 0 and 1 and assume a metallic electrode with flat DOS and reorganization energy (λ) for $[Ru(NH_3)_6]^{3+/2+}$ of 1 eV [45,47,48]. Thus, the total current can be expressed as:

$$i = i_{an} - i_{cat} \qquad \text{(Eq. 3)}$$

$$i_{an} = nF \cdot C_{red} \cdot k_{an} = nF \cdot C_{red} \cdot k_{max} \cdot \int W_{red}(E) \cdot f(E)_{unoccupied} \, \partial E \qquad \text{(Eq. 4)}$$

$$i_{cat} = nF \cdot C_{ox} \cdot k_{cat} = nF \cdot C_{ox} \cdot k_{max} \cdot \int W_{ox}(E) \cdot f(E)_{occupied} \, \partial E \qquad \text{(Eq. 5)}$$

where $n = 1$ is the number of electrons in the reaction, F is Faraday's constant, C_{red} is the concentration of $[Ru(NH_3)_6]^{2+}$ at the electrode surface, and C_{ox} is the concentration of $[Ru(NH_3)_6]^{3+}$ at the electrode surface.

The simulated LSVs were matched to the experimental data recorded on different TMDC thicknesses by using only k_{max} as the fitting parameter, with E_0' set to -0.29 V as determined on a bare gold electrode in SI-8. At the bare gold surface, $k_{max,Au}$ was determined to be at least 2×10^4 cm/s, as shown in Figure S16B. Note that k_{max} values greater than 2×10^4 cm/s yielded simulated LSV curves that were no longer distinguishable (Figure S16C). Our $k_{max,Au}$ value is close to the pre-exponential frequency factor for the adiabatic heterogeneous electron transfer dominated by the reorganization energy predicted by the Marcus-Hush theory (10^4–10^5 cm/s) [49,50] and also to the experimentally determined value (1.1×10^5 cm/s) obtained for $[Ru(NH_3)_6]^{3+/2+}$ on bare gold [51].

Matching simulation to each individual experimental LSV over the kinetic region (up to the 1/3 of the diffusion-limited current) by adjusting k_{max} allows us to estimate the apparent k_{max} on the different layers ($k_{max.nL}$ for *n*L), as shown in Figure 3C-3E for WS_2. The median $k_{max.nL}$ on MoS_2, $MoSe_2$, and WSe_2 surfaces are shown in Figure S17–S19. The $[Ru(NH_3)_6]^{3+}$ reduction kinetics slows down with the increasing number of layers, as shown in Figure 4. This observation agrees with previous work on the HER at 2D TMDC electrodes [21]. The median $k_{max.nL}$ values extracted for all four studied materials, MoS_2, WS_2, $MoSe_2$, and WSe_2, are summarized in Table 1 and plotted versus the layer number in Figure 5A.

The responses on all four materials are similar and indicate a decrease in k_{max} with an increase in layer thickness, as shown in Figure 5A, except for $k_{max.2L}$ for WSe_2, which is significantly larger compared to the other TMDCs studied, although it remains unclear why this is the case. According to the Gerischer model for heterogeneous electron transfer, the prefactor k_{max} scales with the electronic transmission coefficient, which represents the probability of the electron transfer. The electron tunneling barrier arising from the TMDC material itself would reduce the transmission coefficient, and so k_{max}, as the number of layers increases. Previously an electron tunneling barrier model has been used to evaluate photocurrents obtained for 2D MoS_2 in a bottom-contact configuration [52], and has also been used to assess the HER kinetics on mono and few-layer MoS_2 [21]. Therefore, assuming that tunneling is the dominant process leading to a decrease in k_{max}, the $k_{max.nL}$ corresponding to *n*L TMDC can be described as:

$$k_{max.nL} = k_{max.Au} \cdot \exp(-\beta \cdot h \cdot n) \qquad \text{(Eq. 6)}$$

where β is the tunneling decay constant, h is the thickness of the TMDCs layer (h = 6.15 Å for MoS_2, 6.47 Å for $MoSe_2$, 6.16 Å for WS_2 and 7.00 Å for WSe_2) [7], n is the number of TMDCs layers. Diagram of tunnelling barrier can be found in Figure S22.

The β values for $[Ru(NH_3)_6]^{3+}$ reduction on different layer stacks for MoS_2, $MoSe_2$, WS_2, and WSe_2 obtained from Eq. 6 are reported in Table 1. The four different TMDCs have tunneling decay constants in the range 1.0 - 0.4 $Å^{-1}$, which vary significantly depending on total thickness. Our β values are consistent for 2D TMDCs, which have previously been estimated to have tunneling decay constants of 0.512 $Å^{-1}$ [53].

	$k_{max.1L}$ (cm/s)	$k_{max.2L}$ (cm/s)	$k_{max.3L}$ (cm/s)	$\beta_{Au\text{-}1L}$ ($Å^{-1}$)	$\beta_{Au\text{-}2L}$ ($Å^{-1}$)	$\beta_{Au\text{-}3L}$ ($Å^{-1}$)
MoS_2	250	7.5	1.5	0.71	0.64	0.52
$MoSe_2$	560	26	12	0.55	0.51	0.38
WS_2	43	2.0	0.34	1.00	0.75	0.59
WSe_2	140	120	0.92	0.71	0.36	0.48

Table 1: Median prefactor, k_{max}, and tunneling decay constant, β, evolution with the number of TMDCs layers

The data in Table 1 show that the tunneling decay constant, *β,* decreases with increasing numbers of layers for all four TMDCs. However, $k_{max,nL}$ values do not follow an exponential decay with increased layer thickness as we might expect if each additional layer added an identical electron tunneling barrier, as shown in Figure 5A.

Instead, the kinetics are faster for a larger number of layers than would be predicted by a tunneling model with a constant β.

The electronic band structure of TMDCs depends on the number of stacked layers [54–56]. The band gap of MoS_2, $MoSe_2$, WS_2, and WSe_2 increases with the decreasing layer number (<5L) due to strong quantum confinement in thin layers [56,57]. The larger band gap of thinner layers should therefore lead to an increase in the tunneling barrier height, and therefore larger tunneling decay constants (β). Conversely, the smaller band gap of thicker layers should lead to smaller tunneling decay constants. Diagrams of tunnelling barriers presented Figure S22 illustrate changes of tunnelling barrier with number of layers stacked. Indeed, the derived tunneling decay constants listed in Table 1 agree with this trend.

The β_{Au-nL} values describe n-layers of TMDCs acting as a single tunneling barrier, thus β_{Au-nL} can be compared with the band gaps reported for *n* layers of TMDCs (also displayed in Table S5) [7]. From Table S5, we observe a correlation between β_{Au-nL} values and band gap on the different layer thickness of TMDCs. For instance, of the TMDCs we studied, WS_2 has the largest band gap and WS_2 also showed the largest tunneling decay constant, β_{Au-nL}, values. Likewise, of the materials we considered, $MoSe_2$ has the smallest band gap and also shows the smallest β_{Au-nL} values. In fact, we observe a strong correlation between the band gap values sourced from literature and our measured tunneling decay constant, β_{Au-nL}, values, as shown in Figure 5B. Our findings are supported by recent work by Lee *et al.,* who experimentally determined the tunneling barrier height on the different number of layers (1-5L) of MoS_2 on gold using conducting AFM [58]. The barrier height maximum is observed at 1L, then decreases and stabilizes at >5L, in good agreement with values reported in Table 1 obtained using an outer-sphere redox probe.

The electrochemical response on a few-layer 2D TMDCs, in a bottom-contacted configuration, depends on the electron transport process through the TMDC layers. This electron transport is strongly influenced by the electronic structure of the 2D TMDCs, with larger band gaps resulting in a larger decrease in k_{max} with each additional layer, and therefore a higher electron tunneling barrier. However, 2D TMDCs with a fewer number of stacked layers show faster electron transport kinetics due to a narrower tunneling barrier, despite having a larger tunneling decay constant. As a consequence, bottom-contacted TMDC samples with a heterogeneous number of stacked layers will produce an electrochemical response dominated by the monolayer activity at lower overpotentials but with increasing activity of thicker layers at higher overpotentials (assuming there is no diffusional overlap). Our findings suggest that the electrochemical response of TMDC electrode surfaces is profoundly affected by the mode of contact established on electrodes. This has implications for the interpretation of electrochemical and, importantly, electrocatalytic experiments at TMDC nanoarchitectures. Through-layer or within-layer electron transport must be considered when interpreting the performance of TMDC materials in the HER or other reactions of relevance to advanced electrochemical applications.

4. Conclusions

SECCM has been used to quantify the effect of the number of stacked layers of 2D TMDCs (MoS_2, $MoSe_2$, WS_2, WSe_2) on the electrochemical response of the $[Ru(NH_3)_6]^{3+/2+}$ redox couple. Combining SECCM and AFM allowed us to precisely determine the exact nature of the underlying 2D material at each sample point, and to quantify the electrochemical response on the different numbers of layers. There is a significant difference in the electrochemical response on the different numbers of stacked layers, with more facile kinetics observed on thinner stacks of all four materials.

The kinetic dependence was assessed by comparison with a finite element simulation that coupled the diffusional mass transport of $[Ru(NH_3)_6]^{3+/2}$ in the nanopipette probe with the Gerischer description of the electrochemical kinetics. We quantified the rate of electron transfer on a different number of stacked layers of four TMDCs by fitting a simulated response to the experimentally measured LSVs by only varying the maximum kinetic rate, k_{max}. MoS_2, $MoSe_2$, WS_2, and WSe_2 all show a decrease in the electron transfer rate constant as the number of layers increases.

Trends in the electron transfer rates were described by considering an electron tunneling barrier arising from the TMDC itself. This allowed us to extract the apparent tunneling decay constants, β, which range over 1.0 - 0.4 $Å^{-1}$ across all TMDC materials tested; these values are consistent with those reported for tunneling decay constants of 2D TMDCs by other groups [53,58].

We observe that the prefactor, k_{max}, decays more slowly than we would expect if each additional layer added an identical electron tunneling barrier. Thus, the previously reported tunneling barrier model for HER on a few-layer MoS_2, where tunneling decay constant was unaffected by the number of TMDCs layers [21], is insufficient to explain our experimental data. The correlation observed between band gap and tunneling decay constant suggest that non-exponential decay of rate constants is due to a change in the electronic properties of the tunneling barrier, resulting from band gap changes as a function of the number of stacked layers of TMDCs. Therefore, the variation on the electronic structure of the 2D material affects the electron transport to such an extent that we can observe the effect in our electrochemical measurements.

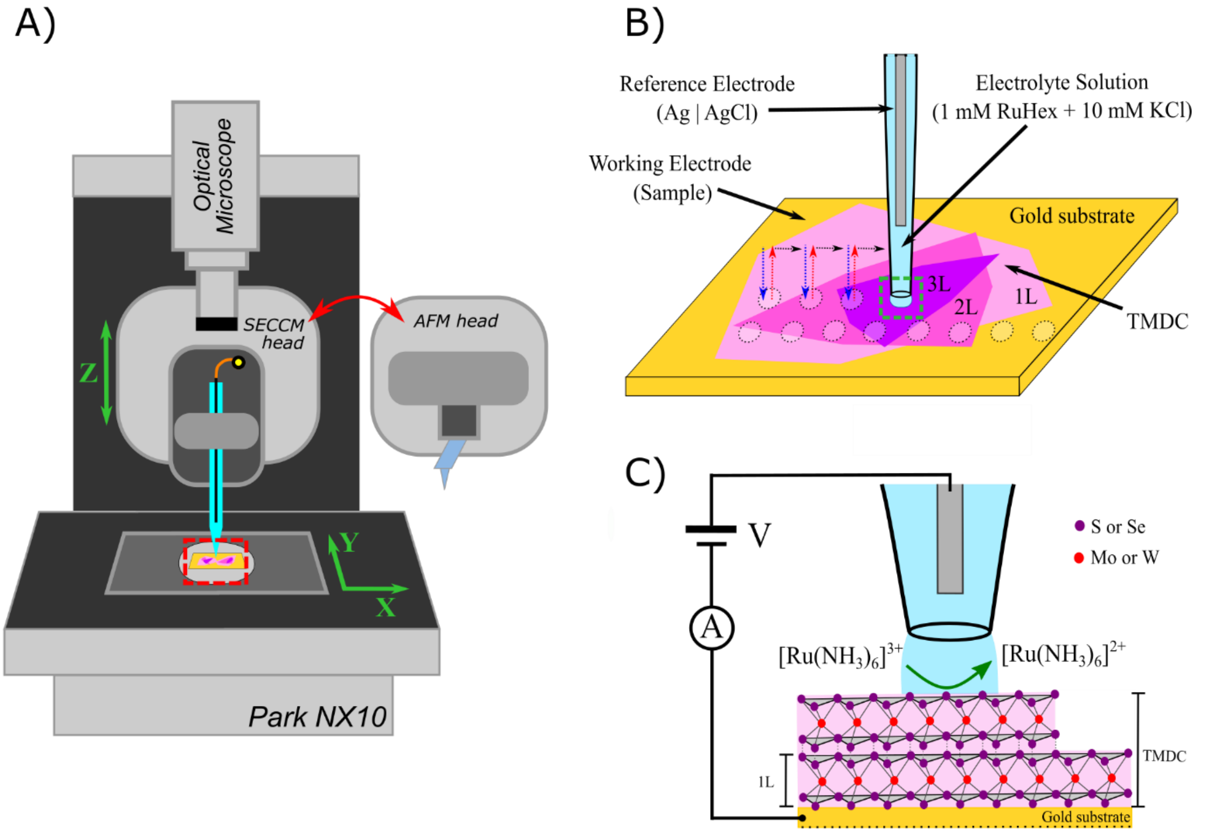

Figure 1: **(A)** Schematic of the ParkSystems NX10 experimental setup, featuring an SECCM probe and an exchangeable AFM probe head **(B)** Schematic of the SECCM nanopipette probe mapping the electrochemical response of the TMDC surface. **(C)** Schematic of the nanodroplet-based electrochemical cell (located at the end of an SECCM probe), showing the electrochemical reaction taking place at TMDCs surface, the TMDC structure, and the electrical contact with the Au substrate.

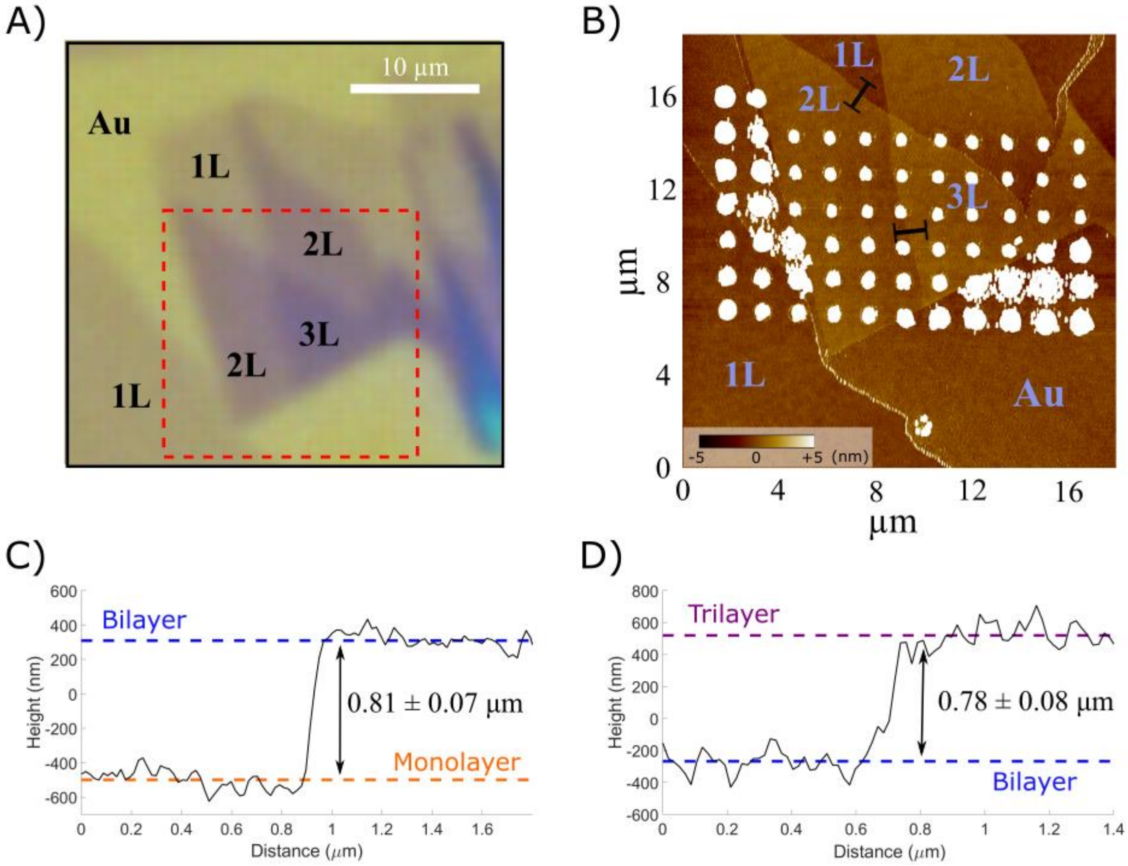

Figure 2: A) Optical image of $MoSe_2$ crystals with differing number of layers. **B)** AFM image of a region depicted by the red rectangle in part A. The AFM was taken after the SECCM measurements and therefore revealed the electrolyte residues at the areas of contact between the droplet and surface. **C)** and **D)** line profiles of 1L/2L and 2L/3L boundaries, respectively, taken from areas shown by black lines in B). Step-height was calculated as the difference of the average terrace height (dashed colored lines).

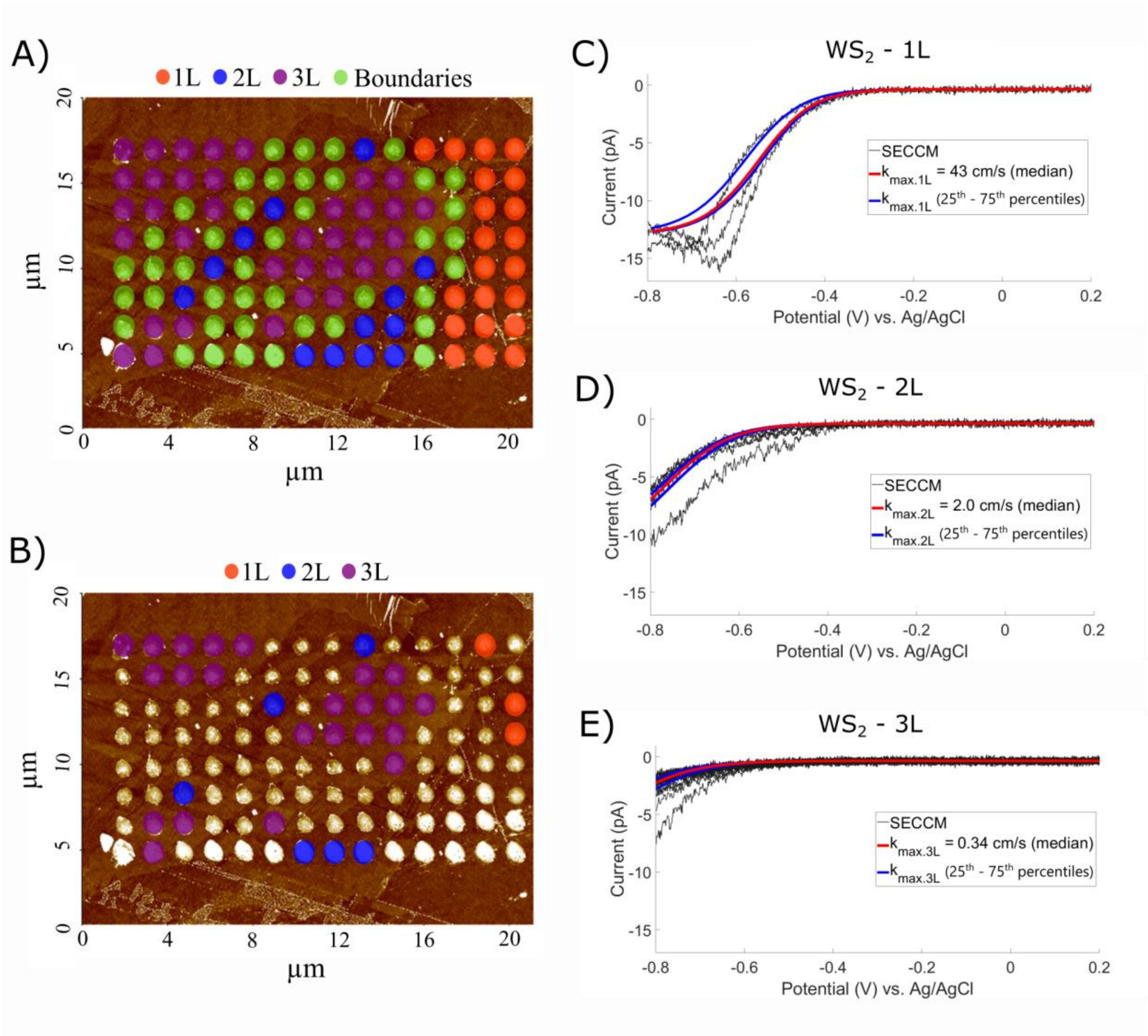

Figure 3: A) Color-coded surface-type assignment in the AFM image showing the +SECCM grid on WS_2. **B)** Color-coded surface-type assignment in the same AFM image, excluding measurements at defects and boundaries. **C)**, **D)** and **E)** LSVs of $[Ru(NH_3)_6]^{3+}$ reduction on 1L, 2L, and 3L from the points shown in B (black traces). Simulated response corresponding to the median k_{max} fitted in red and simulated response corresponding to 25th and 75th percentiles of k_{max} fitting in blue. Dataset formed by 3, 6 and 23 fitted LSVs with k_{max} values for 1L, 2L and 3L respectively.

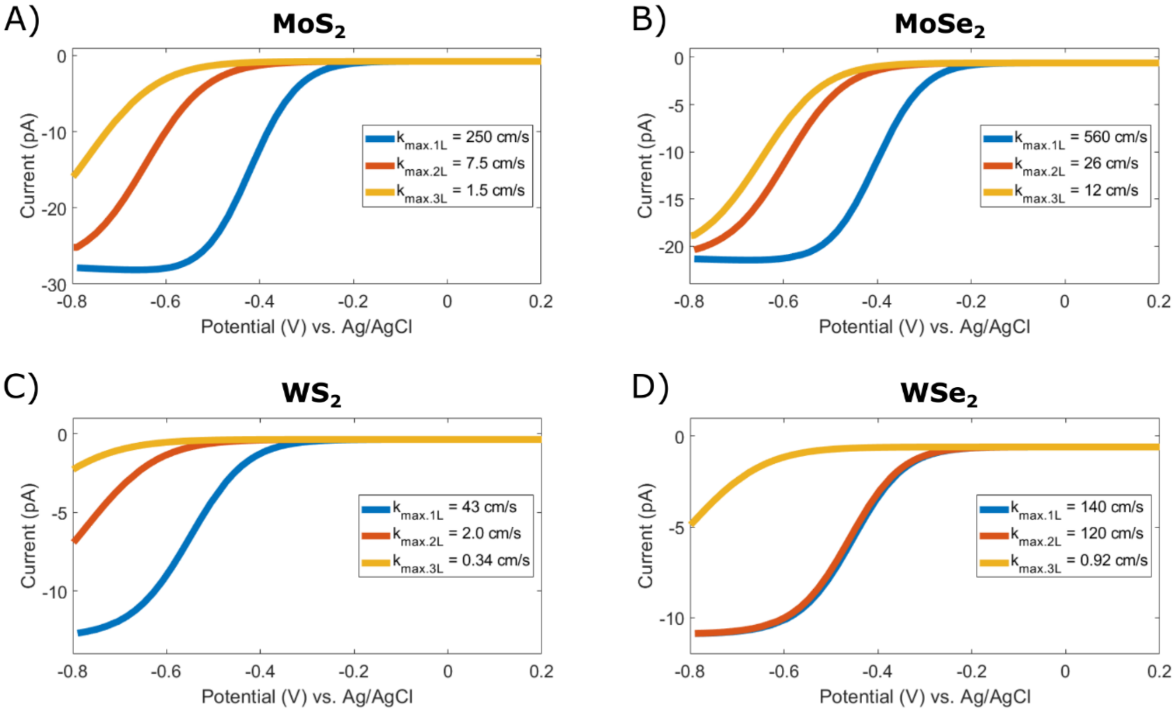

Figure 4: Simulated LSVs with median $k_{max.nL}$ extracted from fitting recorded LSVs on 1L, 2L, and 3L of **A)** MoS_2 **B)** $MoSe_2$ **C)** WS_2 and **D)** WSe_2. Each TMDC displayed a different limiting current according to variation of the observed droplet size, which explains the varying scale of the y-axes.

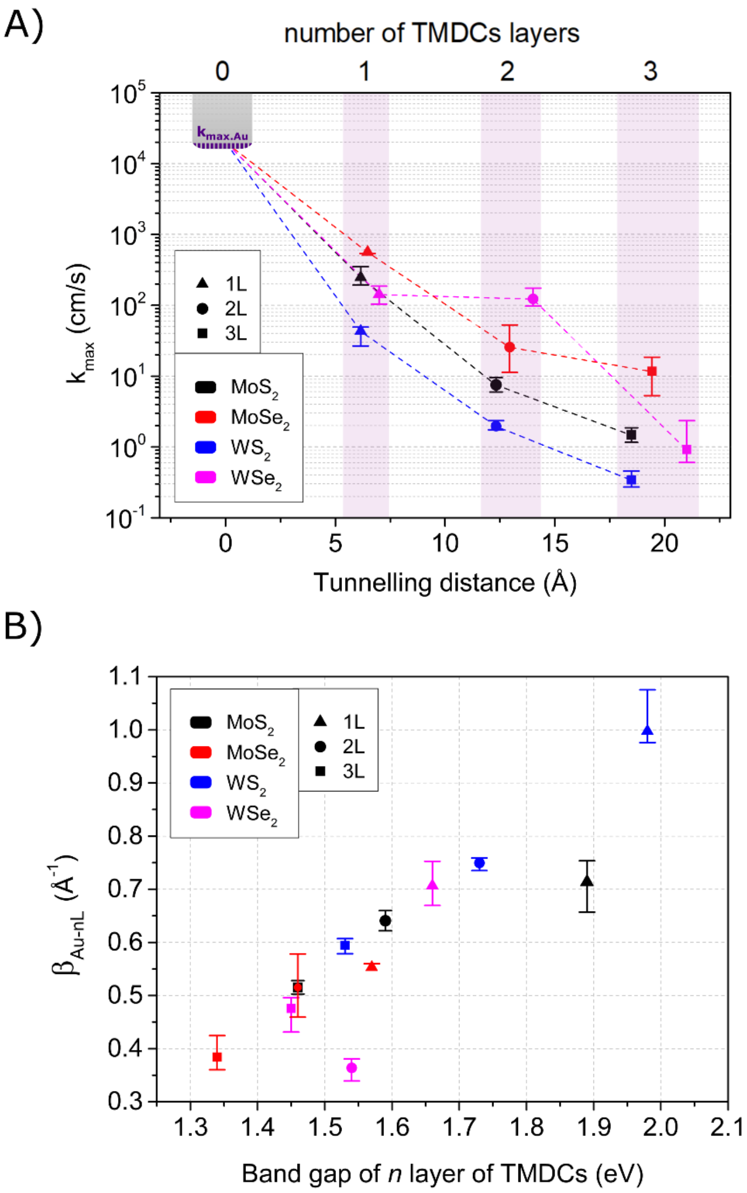

Figure 5: A) k_{max} values determined from fitting simulation to experimental data for different layer thickness. Solid points correspond to each k_{max} value and dashed lines are displayed to guide the eye. Error bar correspond to k_{max} values for 25th and 75th percentiles. **B)** β_{Au-nL} values plotted against band gap for 1-, 2-, and 3-layer MoS_2, $MoSe_2$, WS_2, and WSe_2 [7]. Error bar correspond to β_{Au-nL} derived from k_{max} values for 25th and 75th percentiles. Note some surface types have a limited dataset points and percentile might not be representative of distribution, see table S1.

Declaration of Competing Interest

The authors declare that they have no known competing financial interests or personal relationships that could have appeared to influence the work reported in this paper.

Acknowledgment

We acknowledge parkAFM for loan of the NX10 AFM instrument. M.B. acknowledges the School of Chemsitry, Trinity College Dublin for funding of his PhD.

Apendix A. Supplementary Information

Suplementary information text file is linked to this article.

References

[1] S. Manzeli, D. Ovchinnikov, D. Pasquier, O. V. Yazyev, A. Kis, 2D transition metal dichalcogenides, Nat. Rev. Mater. 2 (2017) 17033–17048, DOI: https://doi.org/10.1038/natrevmats.2017.33

[2] Q. H. Wang, K. Kalantar-Zadeh, A. Kis, J. N. Coleman, M. S. Strano, Electronics and optoelectronics of two-dimensional transition metal dichalcogenides, Nat. Nanotechnol. 7 (2012) 699–712, DOI: https://doi.org/10.1038/nnano.2012.193

[3] W. Choi, N. Choudhary, G. H. Han, J. Park, D. Akinwande, Y. H. Lee, Recent development of two-dimensional transition metal dichalcogenides and their

applications, Mater. Today 20 (2017) 116–130, DOI: https://doi.org/10.1016/j.mattod.2016.10.002

[4] E. Pomerantseva, F. Bonaccorso, X. Feng, Y. Cui, Y. Gogotsi, Energy storage: The future enabled by nanomaterials, Science 366 (2019) 969, DOI: https://doi.org/10.1126/science.aan8285

[5] M. Ahmadi, O. Zabihi, S. Jeon, M. Yoonessi, A. Dasari, S. Ramakrishna, M. J. Naebe, 2D transition metal dichalcogenide nanomaterials: advances, opportunities, and challenges in multi-functional polymer nanocomposites, Mater. Chem. A 8 (2020) 8, 845–883, DOI: https://doi.org/10.1039/C9TA10130F

[6] Z. Wei, B. Li, C. Xia, Y. Cui, J. He, J. B. Xia, J. Li, Various Structures of 2D Transition-Metal Dichalcogenides and Their Applications, Small Methods 2 (2018) 1800094, DOI: https://doi.org/10.1002/smtd.201800094

[7] M. Velický, P. S. Toth, From two-dimensional materials to their heterostructures: An electrochemist's perspective, Appl. Mater. Today 8 (2017) 68–103, DOI: https://doi.org/10.1016/j.apmt.2017.05.003

[8] X. Chia, A. Y. S. Eng, A. Ambrosi, S. M. Tan, M. Pumera, Electrochemistry of Nanostructured Layered Transition-Metal Dichalcogenides, Chem. Rev. 115 (2015) 11941–11966, DOI: https://doi.org/10.1021/acs.chemrev.5b00287

[9] M. Chhowalla, H. S. Shin, G. Eda, L. J. Li, K. P. Loh, H. Zhang, The chemistry of two-dimensional layered transition metal dichalcogenide nanosheets, Nat. Chem. 5 (2013) 263–275, DOI: https://doi.org/10.1038/nchem.1589

[10] T. Stephenson, Z. Li, B. Olsen, D. Mitlin, Lithium ion battery applications of

molybdenum disulfide (MoS_2) nanocomposites, Energy Environ. Sci. 7 (2014) 209–231, DOI: https://doi.org/10.1039/C3EE42591F

[11] S. Ratha, C. S. Rout, Supercapacitor Electrodes Based on Layered Tungsten Disulfide-Reduced Graphene Oxide Hybrids Synthesized by a Facile Hydrothermal Method, ACS Appl. Mater. Interfaces 5 (2013) 11427–11433, DOI: https://doi.org/10.1021/am403663f

[12] E. G. S. Firmiano, A. C. Rabelo, C. J. Dalmaschio, A. N. Pinheiro, E. C. Pereira, W. H. Schreiner, E. R. Leite, Supercapacitor Electrodes Obtained by Directly Bonding 2D MoS_2 on Reduced Graphene Oxide, Adv. Energy Mater. 4 (2014) 1301380, DOI: https://doi.org/10.1002/aenm.201301380

[13] Z. Zhu, H. Yin, C. T. He, M. Al-Mamun, P. Liu, L. Jiang, Y. Zhao, Y. Wang, H. G. Yang, Z. Tang, D. Wang, X. M. Chen, H. Zhao, Ultrathin Transition Metal Dichalcogenide/3d Metal Hydroxide Hybridized Nanosheets to Enhance Hydrogen Evolution Activity, Adv. Mater. 30 (2018) 1–7, DOI: https://doi.org/10.1002/adma.201801171

[14] Q. Fu, J. Han, X. Wang, P. Xu, T. Yao, J. Zhong, W. Zhong, S. Liu, T. Gao, Z. Zhang, L. Xu, B. Song, 2D Transition Metal Dichalcogenides: Design, Modulation, and Challenges in Electrocatalysis, Adv. Mater. 33 (2020) 1907818, DOI: https://doi.org/10.1002/adma.201907818

[15] L. Lin, P. Sherrell, Y. Liu, W. Lei, S. Zhang, H. Zhang, G. G. Wallace, J. Chen, Engineered 2D Transition Metal Dichalcogenides—A Vision of Viable Hydrogen Evolution Reaction Catalysis, Adv. Energy Mater. 10 (2020) 1903870, DOI: https://doi.org/10.1002/aenm.201903870

[16] Q. Lu, Y. Yu, Q. Ma, B. Chen, H. Zhang, 2D Transition-Metal-Dichalcogenide-

Nanosheet-Based Composites for Photocatalytic and Electrocatalytic Hydrogen Evolution Reactions, Adv. Mater. 28 (2016) 1917–1933, DOI: https://doi.org/10.1002/adma.201503270

[17] S. M. Tan, A. Ambrosi, Z. Sofer, Š. Huber, D. Sedmidubský, M. Pumera, Pristine Basal- and Edge-Plane-Oriented Molybdenite MoS_2 Exhibiting Highly Anisotropic Properties, Chem. Eur. J. 21 (2015) 7170–7178, DOI: https://doi.org/10.1002/chem.201500435

[18] M. Velický, M. A. Bissett, P. S. Toth, H. V. Patten, S. D. Worrall, A. N. J. Rodgers, E. W. Hill, I. A. Kinloch, K. S. Novoselov, T. Georgiou, L. Britnell, R. A. W. Dryfe, Electron transfer kinetics on natural crystals of MoS_2 and graphite, Phys. Chem. Chem. Phys. 17 (2015) 17844–17853, DOI: https://doi.org/10.1039/C5CP02490K

[19] T. F. Jaramillo, K. P. Jørgensen, J. Bonde, J. H. Nielsen, S. Horch, I. Chorkendorff, Identification of Active Edge Sites for Electrochemical H_2 Evolution from MoS_2 Nanocatalysts, Science 317 (2007) 100–102, DOI: https://doi.org/10.1126/science.1141483

[20] M. Velický, G. E. Donnelly, W. R. Hendren, S. McFarland, D. Scullion, W. J. I. Debenedetti, G. C. Correa, Y. Han, A. J. Wain, M. A. Hines, D. A. Muller, K. S. Novoselov, H. D. Abruna, R. M. Bowman, E. J. G. Santos, F. Huang, Mechanism of Gold-Assisted Exfoliation of Centimeter-Sized Transition-Metal Dichalcogenide Monolayers, ACS Nano 12 (2018) 10463–10472, DOI: https://doi.org/10.1021/acsnano.8b06101

[21] Y. Yu, S. Y. Huang, Y. Li, S. N. Steinmann, W. Yang, L. Cao, Layer-Dependent Electrocatalysis of MoS_2 for Hydrogen Evolution, Nano Lett. 14

(2014) 553–558, DOI: https://doi.org/10.1021/nl403620g

[22] S. B. Desai, S. R. Madhvapathy, M. Amani, D. Kiriya, M. Hettick, M. Tosun, Y. Zhou, M. Dubey, J. W. Ager, D. Chrzan, A. Javey, Gold-Mediated Exfoliation of Ultralarge Optoelectronically-Perfect Monolayers, Adv. Mater. 28 (2016) 4053–4058, DOI: https://doi.org/10.1002/adma.201506171

[23] G. A. Magda, J. Petõ, G. Dobrik, C. Hwang, L. P. Biró, L. Tapasztó, Exfoliation of large-area transition metal chalcogenide single layers, Sci. Rep. 5 (2015) 14714, DOI: https://doi.org/10.1038/srep14714

[24] C. L. Bentley, M. Kang, P. R. Unwin, Nanoscale Surface Structure–Activity in Electrochemistry and Electrocatalysis, J. Am. Chem. Soc. 141 (2019) 2179–2193, DOI: https://doi.org/10.1021/jacs.8b09828

[25] C. L. Bentley, J. Edmondson, G. N. Meloni, D. Perry, V. Shkirskiy, P. R. Unwin, Nanoscale Electrochemical Mapping, Anal. Chem. 91 (2019) 84–108, DOI: https://doi.org/10.1021/acs.analchem.8b05235

[26] M. E. Snowden, A. G. Güell, S. C. S. Lai, K. McKelvey, N. Ebejer, M. A. O'Connell, A. W. Colburn, P. R. Unwin, Scanning Electrochemical Cell Microscopy: Theory and Experiment for Quantitative High Resolution Spatially-Resolved Voltammetry and Simultaneous Ion-Conductance Measurements, Anal. Chem. 84 (2012) 2483–2491, DOI: https://doi.org/10.1021/ac203195h

[27] N. Ebejer, A. G. Güell, S. C. S. Lai, K. McKelvey, M. E. Snowden, P. R. Unwin, Scanning Electrochemical Cell Microscopy: A Versatile Technique for Nanoscale Electrochemistry and Functional Imaging, Ann. Rev. Anal. Chem. 6 (2013) 329–351, DOI: https://doi.org/10.1146/annurev-anchem-062012-092650

[28] N. Ebejer, M. Schnippering, A. W. Colburn, M. A. Edwards, P. R. Unwin, Localized High Resolution Electrochemistry and Multifunctional Imaging: Scanning Electrochemical Cell Microscopy, Anal. Chem. 82 (2010) 9141–9145, DOI: https://doi.org/10.1021/ac102191u

[29] C. L. Bentley, M. Kang, F. M. Maddar, F. Li, M. Walker, J. Zhang, P. R. Unwin, Electrochemical maps and movies of the hydrogen evolution reaction on natural crystals of molybdenite (MoS_2): basal *vs.* edge plane activity, Chem. Sci. 8 (2017) 6583–6593, DOI: https://doi.org/10.1039/C7SC02545A

[30] B. Tao, P. R. Unwin, C. L. Bentley, Nanoscale Variations in the Electrocatalytic Activity of Layered Transition-Metal Dichalcogenides, J. Phys. Chem. C 124 (2020) 789-798, DOI: https://doi.org/10.1021/acs.jpcc.9b10279

[31] Y. Takahashi, Y. Kobayashi, Z. Wang, Y. Ito, M. Ota, H. Ida, A. Kumatani, K. Miyazawa, T. Fujita, H. Shiku, Y. E. Korchev, Y. Miyata, T. Fukuma, M. Chen, T. Matsue, High-Resolution Electrochemical Mapping of the Hydrogen Evolution Reaction on Transition-Metal Dichalcogenide Nanosheets, Angew. Chemie - Int. Ed. 59 (2020) 3601–3608, DOI: https://doi.org/10.1002/ange.201912863

[32] M. Velický, M. A. Bissett, C. R. Woods, P. S. Toth, T. Georgiou, I. A. Kinloch, K. S. Novoselov, R. A. W. Dryfe, Photoelectrochemistry of Pristine Mono- and Few-Layer MoS_2, Nano Lett. 16 (2016) 2023–2032, DOI: https://doi.org/10.1021/acs.nanolett.5b05317

[33] W. Liao, S. Zhao, F. Li, C. Wang, Y. Ge, H. Wang, S. Wang, H. Zhang, Interface engineering of two-dimensional transition metal dichalcogenides towards next-generation electronic devices: recent advances and challenges,

Nanoscale Horiz. 5 (2020) 787, DOI: https://doi.org/10.1039/C9NH00743A

[34] J. C. McGlynn, T. Dankwort, L. Kienle, N. A. G. Bandeira, J. P. Fraser, E. K. Gibson, I. Cascallana-Matías, K. Kamarás, M. D. Symes, H. N. Miras, A. Y. Ganin, The rapid electrochemical activation of $MoTe_2$ for the hydrogen evolution reaction, Nat. Commun. 10 (2019) 4916, DOI: https://doi.org/10.1038/s41467-019-12831-0

[35] X. Li, C. Batchelor-McAuley, E. Laborda, R.G. Compton, Aqueous Voltammetry in the Near Absence of Electrolyte, Chem. Eur. J. 23 (2017) 15222 – 15226, DOI: https://doi.org/10.1002/chem.201703525

[36] N. S. Taghavi, P. Gant, P. Huang, I. Niehues, R. Schmidt, S. M. Vasconcellos, R. Bratschitsch, M. García-Hernández, R. Frisenda, A. Castellanos-Gomez, Thickness determination of MoS_2, $MoSe_2$, WS_2 and WSe_2 on transparent stamps used for deterministic transfer of 2D materials, Nano Res. 12 (2019) 1691–1695, DOI: https://doi.org/10.1007/s12274-019-2424-6

[37] J. C. Shaw, H. Zhou, Y. Chen, N. O. Weiss, Y. Liu, Y. Huang, X. Duan, Chemical vapor deposition growth of monolayer $MoSe_2$ nanosheets, Nano Res. 7 (2014) 511–517, DOI: https://doi.org/10.1007/s12274-014-0417-z

[38] J. Park, M. S. Kim, E. Cha, J. Kim, W. Choi, Synthesis of uniform single layer WS_2 for tunable photoluminescence, Sci. Rep. 7 (2017) 16121, DOI: https://doi.org/10.1038/s41598-017-16251-2

[39] B. Liu, M. Fathi, L. Chen, A. Abbas, Y. Ma, C. Zhou, Chemical Vapor Deposition Growth of Monolayer WSe_2 with Tunable Device Characteristics and Growth Mechanism Study, ACS Nano 9 (2015) 6119–6127, DOI: https://doi.org/10.1021/acsnano.5b01301

[40] Y. Zhang, H. Li, H. Wang, R. Liu, S. L. Zhang, Z. J. Qiu, On Valence-Band Splitting in Layered MoS_2, ACS Nano 9 (2015) 8514–8519, DOI: https://doi.org/10.1021/acsnano.5b03505

[41] P. K. Chow, E. Singh, B. C. Viana, J. Gao, J. Luo, J. Li, Z. Lin, A. L. Elías, Y. Shi, Z. Wang, M. Terrones, N. Koratkar, Wetting of Mono and Few-Layered WS_2 and MoS_2 Films Supported on Si/SiO_2 Substrates, ACS Nano 9 (2015) 3023–3031, DOI: https://doi.org/10.1021/nn5072073

[42] A. Kozbial, X. Gong, H. Liu, L. Li, Langmuir, Understanding the Intrinsic Water Wettability of Molybdenum Disulfide (MoS_2), 31 (2015) 8429–8435, DOI: https://doi.org/10.1021/acs.langmuir.5b02057

[43] T. Smith, The hydrophilic nature of a clean gold surface, J. Colloid Interface Sci. 78 (1980) 51−55, DOI: https://doi.org/10.1016/0021-9797(80)90348-3

[44] S. W. Feldberg, Implications of Marcus−Hush Theory for Steady-State Heterogeneous Electron Transfer at an Inlaid Disk Electrode, Anal. Chem. 82 (2010) 5176–5183, DOI: https://doi.org/10.1021/ac1004162

[45] M. Velický, S. Hu, C. R. Woods, P. S. Tóth, V. Zólyomi, A. K. Geim, H. D. Abruña, K. S. Novoselov, R. A. W. Dryfe, Electron Tunneling through Boron Nitride Confirms Marcus–Hush Theory Predictions for Ultramicroelectrodes, ACS Nano 14 (2020) 993–1002, DOI:https://doi.org/10.1021/acsnano.9b08308

[46] R. Memming, Semiconductor Electrochemistry, Wiley-VCH VerlagGmbH & Co.KGaA, 2015, p 127-244 (Second Edition), DOI: https://doi.org/10.1023/A:1025744525621

[47] W. J. Royea, T. W. Hamann, B. S. Brunschwig, N. S. A. Lewis, A Comparison

between Interfacial Electron-Transfer Rate Constants at Metallic and Graphite Electrodes, J. Phys. Chem. B 110 (2006) 19433−19442, DOI: https://doi.org/10.1021/jp062141e

[48] S. Ghosh, S. Hammes-Schiffer, Calculation of Electrochemical Reorganization Energies for Redox Molecules at Self-Assembled Monolayer Modified Electrodes, J. Phys. Chem. Lett. 6 (2015) 1−5, DOI: https://doi.org/10.1021/jz5023784

[49] J. T. Hupp, M. J. Weaver, Experimental estimate of the electron-tunneling distance for some outer-sphere electrochemical reactions, J. Phys. Chem. 88 (1984) 1463, DOI: https://doi.org/10.1021/j150652a004

[50] Z. D. He, Y. X. Chen, E. Santos, W. Schmickler, The Pre-exponential Factor in Electrochemistry, Angew. Chem. Int. Ed. 57 (2018) 7948 – 7956, DOI: https://doi.org/10.1002/anie.201800130

[51] A. M. Becka, C. Miller, Electrochemistry at .omega.-hydroxy thiol coated electrodes. 3. Voltage independence of the electron tunneling barrier and measurements of redox kinetics at large overpotentials, J. Phys. Chem. 96 (1992) 2657-2668, DOI: https://doi.org/10.1021/j100185a049

[52] Y. Son, Q. H. Wang, J. A. Paulson, C. J. Shih, A. G. Rajan, K. Tvrdy, S. Kim, B. Alfeeli, R. D. Braatz, M. S. Strano, Layer Number Dependence of MoS_2 Photoconductivity Using Photocurrent Spectral Atomic Force Microscopic Imaging, ACS Nano 9 (2015) 2843–2855, DOI: https://doi.org/10.1021/nn506924j

[53] K. Datta, Q. D. M. Khosru, Simulation of thin-TFETs using transition metal dichalcogenides: effect of material parameters, gate dielectric on electrostatic

device performance, J. Comput. Electron. 16 (2017) 228–239, DOI: https://doi.org/10.1007/s10825-017-0978-7

[54] K. C. Wang, T. K. Stanev, D. Valencia, J. Charles, A. Henning, V. K. Sangwan, A. Lahiri, D. Mejia, P. Sarangapani, M. Povolotskyi, A. Afzalian, J. Maassen, G. Klimeck, M. C. Hersam, L. J. Lauhon, N. P. Stern, T. Kubis, Control of interlayer physics in 2H transition metal dichalcogenides, J. Appl. Phys. 122 (2017) 224302, DOI: https://doi.org/10.1063/1.5005958

[55] J. H. Park, S. Vishwanath, X. Liu, H. Zhou, S. M. Eichfeld, S. K. Fullerton-Shirey, J. A. Robinson, R. M. Feenstra, J. Furdyna, D. Jena, H. G. Xing, A. C. Kummel, Scanning Tunneling Microscopy and Spectroscopy of Air Exposure Effects on Molecular Beam Epitaxy Grown WSe_2 Monolayers and Bilayers, ACS Nano 10 (2016) 4258−4267, DOI: https://doi.org/10.1021/acsnano.5b07698

[56] D. J. Trainer, A. V. Putilov, C. Giorgio, T. Saari, B. Wang, M. Wolak, R. U. Chandrasena, C. Lane, T. R. Chang, H. T. Jeng, H. Lin, F. Kronast, A. X. Gray, X. Xi, J. Nieminen, A. Bansil, M. Iavarone, Inter-Layer Coupling Induced Valence Band Edge Shift in Mono- to Few-Layer MoS_2, Sci Rep 7 (2017) 40559, DOI: https://doi.org/10.1038/srep40559

[57] W. S. Yun, S. W. Han, S. C. Hong, I. G. Kim, J. D. Lee, Thickness and strain effects on electronic structures of transition metal dichalcogenides: 2H-MX2 semiconductors (M = Mo, W; X = S, Se, Te), Phys. Rev. B 85 (2012) 033305, DOI: https://doi.org/10.1103/PhysRevB.85.033305

[58] H. Lee, S. Deshmukh, J. Wen, V. C. Costa, J. S. Schuder, M. Sanchez, A. S. Ichimura, E. Pop, B. Wang, A. K. M. Newaz, Layer-Dependent Interfacial

Transport and Optoelectrical Properties of MoS_2 on Ultraflat Metals, ACS Apl. Mater. Interfaces 11 (2019) 31543−31550, DOI: https://doi.org/10.1021/acsami.9b09868

[59] C. Murray, W. Jolie, J. A. Fischer, J. Hall, C. Efferen, N. Ehlen, A. Grüneis, C. Busse, T. Michely, Comprehensive tunneling spectroscopy of quasifreestanding MoS2 on graphene on Ir(111), Phys. Rev. B 99 (2019) 115434, DOI: https://doi.org/10.1103/PhysRevB.99.115434